# Temperature Dependence of Solid-State Electron Exchanges of Mixed-Valent Ferrocenated Au Monolayer-Protected Clusters

Tessa M. Carducci, Raymond E. Blackwell, and Royce W. Murray*

Kenan Laboratories of Chemistry, University of North Carolina, Chapel Hill, North Carolina 27599, United States

Ⓢ *Supporting Information*

ABSTRACT: Electron transfers (ETs) in mixed-valent ferrocene/ferrocenium materials are ordinarily facile. In contrast, the presence of ~1:1 mixed-valent ferrocenated thiolates in the organothiolate ligand shells of <2 nm diameter Au_{225}, Au_{144}, and Au_{25} monolayer-protected clusters (MPCs) exerts a retarding effect on ET between them at and below room temperature. Near room temperature, in dry samples, bimolecular rate constants for ET between organothiolate-ligated MPCs are diminished by the addition of ferrocenated ligands to their ligand shells. At lower temperatures (down to ~77 K), the thermally activated (Arrhenius) ET process dissipates, and the ET rates become temperature-independent. Among the Au_{225}, Au_{144}, and Au_{25} MPCs, the temperature-independent ET rates fall in the same order as at ambient temperatures: $Au_{225} > Au_{144} > Au_{25}$. The MPC ET activation energy barriers are little changed by the presence of ferrocenated ligands and are primarily determined by the Au nanoparticle core size.
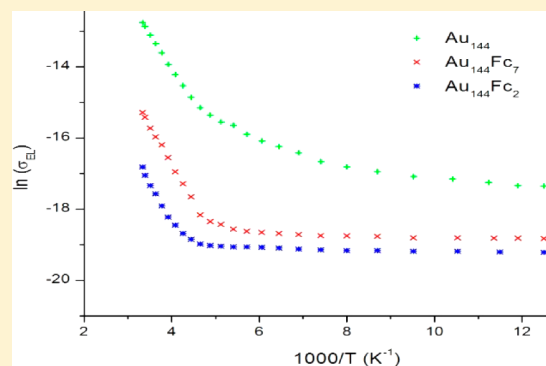
INTRODUCTION

A fundamental understanding of nanoparticles is the foundation for applications of devices made from them. Nanoparticles of varied size can display a wide range of properties. Au monolayer-protected clusters (MPCs) in the 1−2 nm size regime exhibit distinctive electrochemical behaviors. The smallest MPCs (e.g., Au_{25} nanoparticles) are molecule-like, having HOMO−LUMO energy gaps[1] that can be observed in their voltammetry. Slightly larger ones (e.g., Au_{144} and Au_{225}) display electrochemical properties called quantized double-layer (QDL) charging.[2−4] These electrochemical features, as well as solubilities and spectra, are further moderated by the thiolate ligands that can be used to coat the Au MPC core surfaces.[4,5] Inclusion of thiolate ligands with redox or bioactive groups opens the door to further customization of nanoparticles toward specific applications.[4−6]

Functionalization of MPCs with multiple redox ligands, such as ferrocenes, increases the nanoparticle redox capacity to transfer multiple electrons within a small range of potentials. Ferrocenes can be added to the MPC ligand shells by a postsynthesis ligand exchange reaction,[7−9] or the MPCs can be fully ferrocenated when synthesized de novo.[10] Early work[11] showed that functionalization of Au MPCs with a ferrocene (Fc) thiol can lead to multielectron transfer reactions for both freely diffusing nanoparticles and electrode-adsorbed clusters. More recently, Schiffrin and co-workers[12] synthesized 1.8 nm diameter Au MPCs containing 4, 7, or 10 Fc thiolate ligands, using ligand exchanges, and observed their electron transfer (ET) reactions.

Most studies of ETs between ferrocenated Au MPCs have focused on solution-wetted films on electrode surfaces[13−15] and their charge storage capabilities.[16] Ferrocene labels have also been used in combination with Au nanoparticles to enhance current response in sensors.[6,17] However, little is known about how the Fc group might affect electron exchanges of Au clusters as solid-state samples, including their ET behavior at low temperatures.

The present study is of highly monodisperse Au MPCs containing small numbers of ferrocene sites in their ligand shells. In solvent-free dry films, ET reactions between neighboring MPCs and their ferrocene substituents can be induced by mild applied voltage gradients, thereby exhibiting linear current−voltage characteristics.[18] Such studies show that these solid-state conductivities of MPC films are sensitive to the film's mixed-valent state. The corresponding solid-state electron self-exchange rates are the experimental topic of the present paper, with special emphasis on how their rates change over a wide span of temperature (e.g., from room temperature down to 77 K).

Previous electronic conductivity studies of Au MPC films with small, highly monodisperse core sizes were suggested to involve an ET pathway along the ligand chain to progress from Au core to Au core.[19] This process has been described as a bimolecular electron "self-exchange" between MPCs:[20]

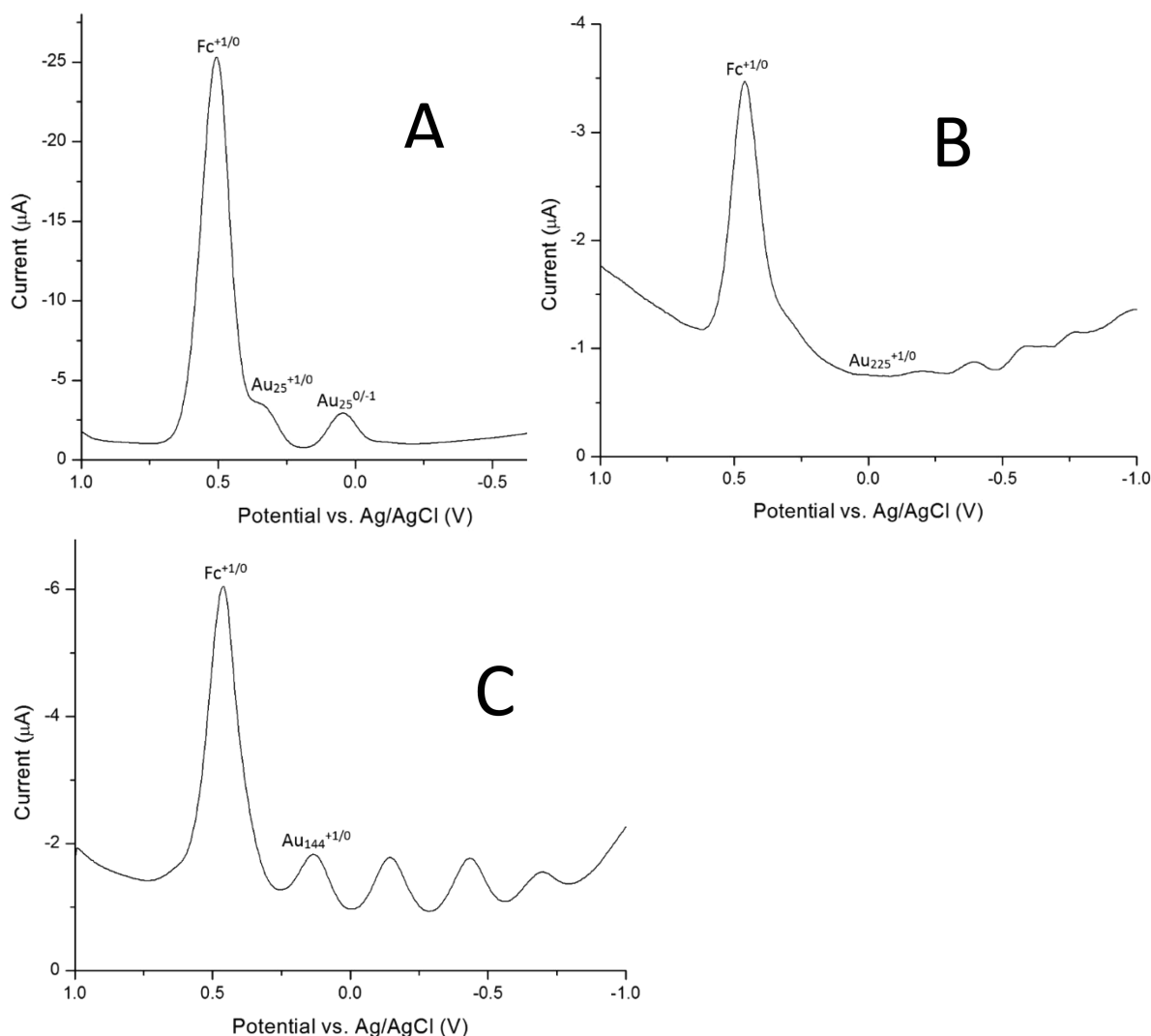$$MPC^Z + MPC^{Z+1} \overset{k_{EX}}{\rightleftharpoons} MPC^{Z+1} + MPC^Z \qquad (1)$$
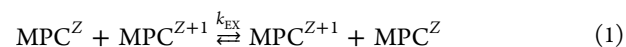
Figure 1. DPV curves for ~1 mM (A) ferrocenated Au_{25}, (B) ferrocenated Au_{144} and (C) ferrocenated Au_{225} in 50 mM Bu_4NClO_4/CH_2Cl_2 at a 0.020 cm² Pt disk. Redox potentials of interest are indicated. Data were obtained with a Pine WaveNano USB potentiostat.

where k_{EX} is the bimolecular nanoparticle electron self-exchange rate constant. In the present study, the MPCs bear multiple Fc thiolate ligands in mixed-valent $Fc^{+1/0}$ form, where the $Fc^{1+/0}$ couple supports multiple electron exchanges so that MPC–MPC core ETs become less prominent in the voltammetry:

$$[Fc(0)MPC^Z + Fc(1+)MPC^Z$$
$$\overset{k_{Fc,EX}}{\rightleftharpoons} Fc(1+)MPC^Z + Fc(0)MPC^Z] \qquad (2)$$
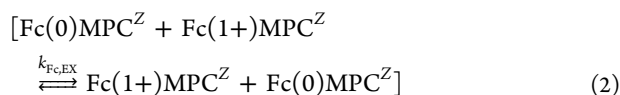
In the reaction shown in eq 2, $k_{Fc,EX}$ is the rate constant of interest. As with any bimolecular process, the contribution of ferrocene ETs to the nanoparticle sample's electronic conductivity (σ_{EL} (ohm⁻¹cm⁻¹)) becomes maximized when the Fc(0) and Fc(1+) populations on the MPCs are equal.

The reported experiments describe electron-hopping conductivities in films of ferrocene-containing Au_{225}, Au_{144}, and Au_{25} nanoparticles from room temperature to cryogenic temperatures. Like non-ferrocenated[18] Au_{144} and Au_{25} MPCs, non-Arrhenius (temperature-independent) ET behavior is observed at low temperatures, indicative of an electron tunneling mechanism.[21] For these studies, we selected three size-purified 1−2 nm diameter Au MPCs: $Au_{225}(SR)_{75}$,

$Au_{144}(SR)_{60}$, and $Au_{25}(SR)_{18}$. For the Au_{225} and Au_{144} nanoparticles, the thiolate ligand SR was $-S(CH_2)_5CH_3$, and for the Au_{25} nanoparticle, SR was $-S(CH_2)_2Ph$. Partial ferrocenation of the thiolate ligand shell was accomplished via ligand exchanges with 6-(ferrocenyl)hexanethiol. Fc–Au MPCs were electrolytically made mixed-valent with respect to the $Fc^{+1/0}$ redox couple. The mixed-valent nanoparticle films were drop-cast from their deaerated, mixed-valent solutions onto interdigitated array electrodes (IDAs) so that the MPC film thicknesses exceeded the IDA finger heights. Voltage biases applied to the IDA finger pairs were used to supply the voltage gradient impetus for electron hopping within the dry mixed-valent nanoparticle films. For notational simplicity, the non-ferrocenated MPCs are denoted as Au_{25}, Au_{144}, and Au_{225} and the ferrocenated versions as $Au_{25}Fc$, $Au_{144}Fc$, and $Au_{225}Fc$.

■ EXPERIMENTAL SECTION

Materials. Hydrogen tetrachloroaurate(III) trihydrate ($HAuCl_4\cdot 3H_2O$) was synthesized according to the literature.[22,23] 1-Hexanethiol ($C_6H_{13}SH$, 95%), 2-phenylethanethiol [$Ph(CH_2)_2SH$, 98%], 6-(ferrocenyl)hexanethiol ($C_{16}H_{21}FeSH$), sodium borohydride ($NaBH_4$, 99%), and tetraoctylammonium bromide (Oct_4NBr, 98%) were purchased from Sigma-Aldrich (St. Louis, MO), tetrabutylammonium perchlorate (Bu_4NClO_4, 99.0%) from Fisher Scientific

(Suwanee, GA) or Fluka (Milwaukee, WI), and Optima-grade toluene, methanol (CH_3OH), acetonitrile (CH_3CN), and dichloromethane (CH_2Cl_2) from Fisher Scientific. Ethanol (absolute, i.e., 200 proof) was purchased from Decon Laboratories, Inc. (King of Prussia, PA).

Synthesis of Au MPCs. The syntheses of $Au_{225}(SC_6H_{13})_{75}$, $Au_{144}(SC_6H_{13})_{60}$, and $Au_{25}(SC_2Ph)_{18}$ as monodisperse nanoparticles were carried out as described previously.[18] Partial ferrocenation of the Au_{225}, Au_{144}, and Au_{25} nanoparticles' ligand shells was achieved through a postsynthesis ligand exchange reaction.[25] Briefly, a solution of as-synthesized nanoparticles (~1 mM) was stirred overnight with 6-(ferrocenyl)hexanethiol in various stoichiometric ratios with the nanoparticle, depending on the desired level of ferrocenation (1–5 fold excess). Free thiol was removed by nanoparticle precipitation by addition of CH_3CN for $Au_{225}Fc$ and $Au_{144}Fc$ and CH_3OH for $Au_{25}Fc$ with recovery of the nanoparticles by centrifugation.

Film Preparation on Interdigitated Array Electrodes. The IDAs used [microfabricated in-house by the Chapel Hill Analytical and Nuclear Laboratory (CHANL)] had 50 interdigitated Au fingers on a glass substrate. Fingers of IDAs made for Au_{225} and Au_{144} measurements were 0.298 cm long and spaced 15 μm apart. IDAs made for Au_{25} samples had 50 interdigitated fingers that were 0.298 cm long and spaced 10 μm apart; the smaller IDA gap was chosen to increase the currents in the conductivity scans. Connections to finger sets were made with soldered wire leads covered with epoxy resin. Films of Au MPCs were drop-cast onto the IDA electrodes from concentrated Au MPC toluene solutions (~10 mg) in one small drop.

■ RESULTS AND DISCUSSION

Characterization of Au MPCs. Differential pulse voltammetry (DPV) curves for synthesized $Au_{25}Fc$, $Au_{144}Fc$, and $Au_{225}Fc$ are shown in Figure 1. Patterns of QDL charging, with uniformly spaced one-electron DPV peaks, are observed for Au_{225}[24] and Au_{144},[3] while Au_{25}[26] nanoparticles display their known HOMO-level doublet of peaks. Superimposed on this characteristic nanoparticle voltammetry is the larger $Fc^{+1/0}$ redox wave for the ferrocenated nanoparticles $Au_{225}Fc$, $Au_{144}Fc$, and $Au_{25}Fc$.

The number of ferrocene-containing ligands per nanoparticle was determined from bulk electrolyses (BEs) at potentials spanning the $Fc^{+1/0}$ wave. BE of ferrocenated Au MPCs was done under Ar in a fine frit-separated three-compartment cell using a Pine WaveNow USB potentiostat and Pt gauze working and reference electrodes in cell compartment 1 and a Pt counter electrode in compartment 3. Compartment 1 contained ~10 mL of 1 mM ferrocenated Au nanoparticles in CH_2Cl_2 and 50 mM Bu_4NClO_4 supporting electrolyte; compartments 2 and 3 contained only 50 mM Bu_4NClO_4/CH_2Cl_2. The electrolysis was halted when the electrolysis current dropped to ~1% of its initial value. The overlap of the redox peak for the $Au_{25}^{+1/0}$ core with that for $Fc^{+1/0}$ was avoided by using double the charge under the more positive half of its peak.

Preparation of Mixed-Valent Au MPCs. BE was used to prepare mixed-valent nanoparticle samples of known ~1:1 molar ratio for $Au_{225}^{+1/0}$, $Au_{225}Fc^{+1/0}$, $Au_{144}Fc^{+1/0}$, and $Au_{25}Fc^{+1/0}$. Mixed-valent $Au_{144}^{+1/0}$, $Au_{25}^{+1/0}$, and $Au_{25}^{0/-1}$ samples were prepared similarly.[18] Mixed valency of non-ferrocenated Au nanoparticles $Au_{225}^{+1/0}$, $Au_{144}^{+1/0}$, $Au_{25}^{+1/0}$, and $Au_{25}^{0/-1}$ refers to the charge state of the nanoparticle core. Electrolysis potentials (E_{elec}) were chosen on the basis of the Nernst equation:[27,28]

$$E_{elec} - E^{Z+1/Z} = 0.059 \log \frac{[MPC^{Z+1}]}{[MPC^Z]} \quad (3)$$

where $E^{Z+1/Z}$ was determined by DPV of the Au MPCs. Mixed valency of the ferrocenated Au nanoparticles $Au_{225}Fc$, $Au_{144}Fc$, and $Au_{25}Fc$ refers to the charge state of the nanoparticle's ferrocene ligand(s). E_{elec} was chosen with reference to the DPV-determined redox potential wave of the ferrocene couple ($E^{+1/0}$):

$$E_{elec} - E^{+1/0} = 0.059 \log \frac{[AuFc^{+1}]}{[AuFc^0]} \quad (4)$$

where $AuFc^{+1/0}$ refers to the $Fc^{+1/0}$ redox wave of the ferrocene-containing Au_{225}, Au_{144}, or Au_{25} nanoparticle. Following BE, the nanoparticle solution was again degassed, and its open-circuit rest potential (vs Ag/AgCl) was measured at a clean Pt wire (Keithley Instruments 610C solid-state electrometer, input impedance $>10^8$ MΩ). The corresponding $MPC^{Z+1/Z}$ and $AuFc^{+1/0}$ population ratios were calculated from post-BE rest potentials and the DPV-determined formal potentials according to eq 3 (non-ferrocenated samples) or 4 (ferrocenated samples).

Mixed-valent samples of Au_{225}, $Au_{225}Fc$, Au_{144}, and $Au_{144}Fc$ MPCs were washed twice with CH_3CN following BE to remove excess electrolyte. Au_{25} and $Au_{25}Fc$ were washed twice with CH_3OH. The wash steps did not alter the open-circuit potentials.

Low-Temperature Electronic Conductivities of Solid-State Au MPC Films. Temperatures of Au MPC films were controlled using a Janus VPF 100 liquid nitrogen cryostat and a Lakeshore 331S temperature controller. IDAs bearing drop-cast nanoparticle films were secured to the heat-conducting sample stage of the cryostat using double-sided tape. The cryostat chamber was evacuated overnight using an Edwards RV8 rotary vane pump; this was required for proper function of the temperature controls and to ensure complete drying of the MPC films. The cryostat cooling chamber was filled with liquid nitrogen and allowed to cool to the minimum temperature (~75 K) prior to initiation of film electronic conductivity measurements. The measurements were done using a home-built two-electrode circuit designed to apply a voltage ramp and measure currents as low as 10^{-10} A (controlled by LabView software). Capacitance was minimized by connecting the circuit directly to the cryostat. Electronic conductivities were calculated from the slopes of linear current−potential plots in a triangular potential scan between 0.25 and −0.25 V with initial and final voltages of 0 V. The 10 V/s scan rate was aimed at avoiding electrostatic counterion migration within the film, as was avoidance of temperatures above 300 K. Conductivity scans were performed at temperature intervals between 2 and 10 K as the IDA electrode temperature was raised in a controlled manner from 77 to 300 K.

The mixed-valent MPC film's electronic conductivity, σ_{EL}, was calculated from the slopes of the current−potential plots according to[20,29]

$$\sigma_{EL} = \left(\frac{d}{A_{total}}\right)\frac{\Delta i}{\Delta E} \quad (5)$$

in which d is the IDA gap and $A_{total} = A_{finger}(N-1)$, where A_{finger} is the area of the walls of facing parallel-plate finger electrodes, with height taken as the maximum conductive MPC film thickness (~1 μm) and length equal to the finger length, and N is the total number of fingers (50). (The current of each interior finger is double that of an end finger.) The ratio d/A_{total} is the geometric cell constant, C_{cell}, which for the IDAs used for

Au_{225} and Au_{144} films was 1.021 cm^{-1} and for Au_{25} films was 0.685 cm^{-1}.

The conductivities of the $Au_{25}Fc$ films were too low to be measured with the home-built circuit, so the resistance at 298 K was measured with a Keithley Instruments 610C solid-state electrometer and multiplied by C_{cell} to estimate values of the same form as σ_{EL} for comparison with other films.

Electronic Conductivity of MPC Films from 77 to 300 K. The σ_{EL} results for the Au MPC films from 77 to 300 K are presented in Figures 2 and 3 as Arrhenius plots. Two regimes of
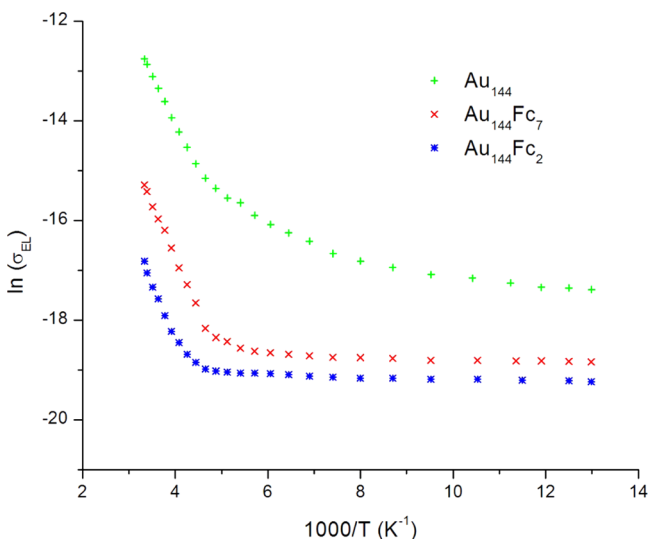

Figure 2. Arrhenius plots of solid-state electronic conductivities of ferrocenated and non-ferrocenated Au_{144} MPC films containing mixed-valent proportions of the MPC$^{+1/0}$ or Fc$^{1+/0}$ (ferrocenated) charge states (see Table 2).
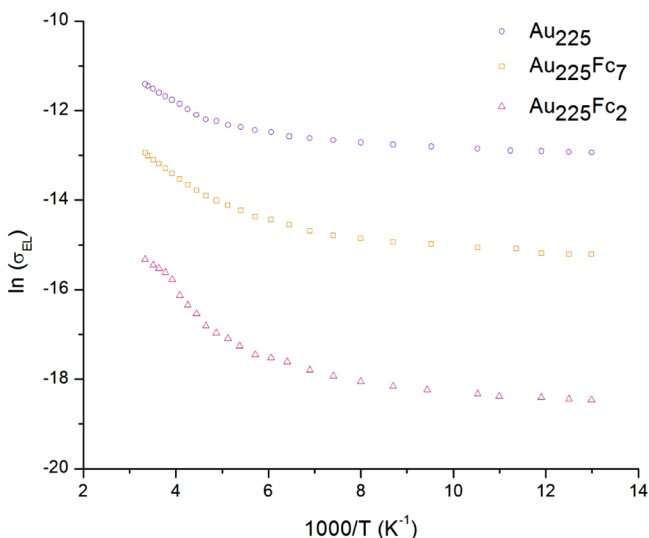

Figure 3. Arrhenius plots of solid-state electronic conductivities of ferrocenated and non- ferrocenated Au_{225} MPC films containing mixed-valent proportions of the MPC$^{+1/0}$ or Fc$^{1+/0}$ (ferrocenated) charge states. (See Table 2).

behavior can be observed. At higher temperatures, the conductivities reflect a thermally activated ET process and strongly temperature-dependent ET rates. At the lowest temperatures, the ET conductivity becomes temperature-independent, characteristic of electron tunneling.[18] In the

thermally activated ET region, the Arrhenius plot is linear such that[19]

$$\ln(\sigma_{EL}) = -\frac{E_A}{RT} - r_0\beta + \ln(\sigma_0) \qquad (6)$$

where E_A is the activation energy for thermally activated ET, β is an electronic coupling term[19] for ET tunneling through the MPC ligand shell, and r_0 is the average edge-to-edge distance between neighboring MPC Au cores. The y-intercept represents an infinite-temperature electronic conductivity.[19,20]

Like previous observations[18] for non-ferrocenated, mixed-valent Au_{144} and Au_{25}, the transition between thermally activated and tunneling ET behavior for mixed-valent Fc–Au MPCs is gradual (Figures 2 and 3). The total current measured at any given temperature represents the sum of the currents arising from all ET processes.[21] In the flattened, lowest-temperature regions of the Arrhenius plots in Figures 2 and 3, the ET conductivity is solely through the mechanism of tunneling. Tunneling currents dominate at low temperatures as energy-activated states are emptied, thermal energy is depleted, and electron hopping is diminished. At higher temperatures, in the thermally activated region, the electron hopping mechanism dominates and the tunneling current becomes a minor contributor, retaining its small value regardless of temperature.

It was previously found[18,30] that in non-ferrocenated Au MPCs the magnitudes of both the thermally activated electron hopping and electron tunneling currents depend on the mixed valency of the particle and on the core size of the particle, those for Au_{144} being larger than Au_{25} (see Figure S-1 in the Supporting Information). The current study further reveals the substantial effects of mixed-valent ferrocene-containing ligands on the nanoparticle ET behavior. The values of the electron hopping conductivity σ_{EL} for mixed-valent ferrocene-containing nanoparticles are substantially smaller than those for the corresponding non-ferrocenated mixed-valent nanoparticles. Obliging ET to occur through the Fc$^{+1/0}$ redox couple seems to help drive the ET behavior into the tunneling regime, suggesting that the ferrocene sites act as kinetic potholes (traps) in the serial electron hopping process.

Consistent with this suggestion, Figures 2 and 3 show that the electron tunneling current varies with the number of ferrocenes in the nanoparticle ligand shell (also see the data for $Au_{25}Fc$ in Table 2). Conversely, ET activation (i.e., E_A) is less changed by the presence or amount of ferrocene ligands; it depends more on the core size. This suggests that the ET conductivity depends on joint contributions from the Au core and the mixed-valent ferrocene sites.

Translation of the ET conductivity data into rate constants requires a model for the average electron hopping distance (δ) in the mixed-valent film. Solid-state densities of nanoparticle samples were determined via pycnometry (Table 1), and core-to-core edge separations δ were calculated according to[18]

$$\delta_{Au_{25}} = 2r_{core} + l_{eff} = 2\left(\frac{(0.7)(10^3)}{\frac{4}{3}\pi C_{film}N_{Avo}}\right)^{1/3} \qquad (7)$$

It should be noted that the nanoparticle separation δ is increased for ferrocenated Au_{225} and Au_{144} nanoparticle films but not measurably for Au_{25} films (Table 1). Using pycnometric distances (rather than earlier-used crystal structure,[31] transmission electron microscopy,[20,32] and/or density functional theory-calculated[33] data) to estimate δ for Au_{144} and Au_{25} was

Table 1. Densities (Obtained by Pycnometry) and Core-to-Core Edge Separation Distances δ (Calculated on the Basis of a Cubic Lattice Model) for Ferrocenated and Non-Ferrocenated Au MPC Solid-State Films

| MPC	density (g mL^{-1})	density (mM)	δ (nm)
Au$_{225}$	4.51	84.4	2.9$_7$
Au$_{225}$Fc$_2$	4.25	79.6	3.0$_3$
Au$_{144}$	3.18	89.8	2.9$_1$
Au$_{144}$Fc$_7$	3.08	84.0	2.9$_8$
Au$_{25}$	1.78	22.7	2.1$_4$
Au$_{25}$Fc$_3$	1.90	22.8	2.1$_4$

favored since the solid-state density includes all factors affecting the average distance between particles, including packing irregularities in the drop-cast films. More importantly, using a single method for calculating δ permits more direct comparison between the present data and those for previously reported[18] non-ferrocenated Au MPC films.

The density information is used with the electron conductivity information in Table 2, where bimolecular electron self-exchange rate constants k_{EX} for the present and previously studied[18] Au MPC films are compared. The translation of density and electronic conductivity values into k_{EX} values is based on the assumption of a cubic lattice film structure (as in previous studies)[18,20,29,30,34]:

$$k_{EX} = \frac{6(10^3)RT\sigma_{EL}}{F^2\delta^2[MPC^{Z+1}][MPC^Z]} \quad (8)$$

where δ is the core edge to core edge separation and $[MPC^{Z+1}]$ and $[MPC^Z]$ are calculated from the Nernst equation.

We have shown previously[18] that k_{EX} for Au$_{144}^{+1/0}$, Au$_{25}^{0/-1}$, and Au$_{25}^{+1/0}$ films is maximized when $[MPC^{Z+1}] = [MPC^Z]$. A further aim here was to determine whether adding ferrocenes to the nanoparticle ligand shell could direct ET to occur via the Fc$^{+1/0}$ redox couple. The data show that indeed the mechanism of ET in mixed-valent ferrocenated MPCs differs from that in non-ferrocenated MPCs. Converting the ferrocene-containing nanoparticle film into a mixed-valent state (with regard to Fc$^{+1/0}$) appears to allow ET via a ferrocene-dependent mechanism similar to that shown in eq 2:
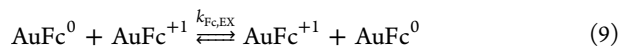
$$AuFc^0 + AuFc^{+1} \underset{}{\overset{k_{Fc,EX}}{\rightleftharpoons}} AuFc^{+1} + AuFc^0 \quad (9)$$

where AuFc$^{+1/0}$ refers to the Fc$^{+1/0}$ redox wave of the ferrocene-containing Au$_{225}$, Au$_{144}$, or Au$_{25}$ nanoparticle. The expression for k_{EX} that follows is also bimolecular:

$$k_{Fc,EX} = \frac{6(10^3)RT\sigma_{EL}}{F^2\delta^2[AuFc^{+1}][AuFc^0]} \quad (10)$$

where $[AuFc^{+1}]$ and $[AuFc^0]$ are calculated using the Nernst equation. Evidence for ferrocene involvement is found in the dependence (for all three Au core sizes studied—225, 144, and 25) of the ET rate constant on the number of ferrocenes present on the nanoparticle. The ET rate constant in Au$_{225}$Fc$_7$ is larger than that for Au$_{225}$Fc$_2$ by over an order of magnitude. The increase in k_{EX} with the number of ferrocenes present in the ligand shell suggests that ET is accelerated by the higher probability of adjacency and favorable orbital overlap[12,35,36] of ferrocenes on neighboring nanoparticles. Multiple ET in solutions of hexanethiolate-protected Au nanoparticles has previously been observed to increase with larger populations of ferrocenes in their ligand shells.[12] While rotational diffusion would be slowed in the solid state, multiple ferrocene sites equally distributed between Fc^{1+} and Fc^0 should still permit multiple ET pathways between neighboring particles. This view is consistent with the lack of change in the ET E_A with the number of ferrocene-containing ligands. The core still plays a role in the ET process, since the E_A for ET strongly responds to the core size of the particle. Probing the roles of the mixed valency of the MPC core and the Fc$^{+1/0}$ redox couple independently is obviously not possible.

■ SUMMARY

We have shown that Fc$^{+1/0}$ ET rates in mixed-valent films of Au$_{225}$Fc, Au$_{25}$Fc, and Au$_{144}$Fc nanoparticles can be observed over a complete range of thermal activation of electron hopping to temperature-independent rates of ET at lower temperatures. The ET rates at lower temperatures mimic the trend at ambient temperatures and increase with the degree of ferrocenation. Adding ferrocene to the ligand shell changes the mechanism of ET from the form of eq 1 to that of eq 9, thus varying both the thermally activated electron hopping current and the tunneling current in response to an applied a potential bias across the film. The degree of ferrocenation also impacts the rate of ET.

Table 2. Activation Energies (E_A), Electron Hopping Conductivities (σ_{EL}), and Self-Exchange Rate Constants (k_{EX}) at 298 K for Mixed-Valent Ferrocenated Au MPC Solid-State Films (Data Are Averages for Three Different Films Having the Same Mixed-Valent Composition)

MPC	$[MPC^{Z+1}]$ or $[Fc^{+1}]$ (%)	E_A (eV)^a	σ_{EL} (Ω^{-1} cm^{-1})	k_{EX} (M^{-1} s^{-1})
Au$_{225}$	50	0.06 ± 0.007	(8.0 ± 6.3) × 10^{-6}	(8.0 ± 6.2) × 10^7
Au$_{225}$Fc$_7$	46	0.063 ± 0.004	(3.7 ± 1.8) × 10^{-6}	(4.0 ± 1.7) × 10^7
Au$_{225}$Fc$_2$	43	0.08 ± 0.04	(2.0 ± 0.8) × 10^{-7}	(2.2 ± 0.9) × 10^6
Au$_{144}$	55	0.17 ± 0.02	(5.9 ± 0.9) × 10^{-6}	(5.6 ± 0.9) × 10^7
Au$_{144}$Fc$_7$	52	0.17 ± 0.02	(1.9 ± 0.3) × 10^{-7}	(1.9 ± 0.3) × 10^6
Au$_{144}$Fc$_2$	76	0.16 ± 0.06	(3.8 ± 1.0) × 10^{-8}	(6.0 ± 1.6) × 10^5
Au$_{25}^{0/-1}$	53	0.38 ± 0.03	(6.3 ± 2.2) × 10^{-7}	(3.8 ± 1.4) × 10^6
Au$_{25}^{+1/0}$	45	0.34 ± 0.09	(6.4 ± 1.2) × 10^{-8}	(3.9 ± 0.7) × 10^5
Au$_{25}$Fc$_3$^{b}	50	could not be quantified	(1.3 ± 0.8) × 10^{-10}	(5.0 ± 3.0) × 10^2
Au$_{25}$Fc$_1$^{b}	52	could not be quantified	(1.4 ± 0.8) × 10^{-10}	(3.7 ± 2.2) × 10^2

$^a E_A$ values were obtained from the linear region (265−300 K). ^{b}Highly resistive films. The resistance at 298 K was measured with an electrometer, and σ_{EL} was calculated by multiplying the resistance by the cell constant of the IDA (C_{cell}).

ASSOCIATED CONTENT

Supporting Information

A previously published[18] figure is re-presented with recalculated values of σ_{EL} based on the improved estimates of δ. This material is available free of charge via the Internet at http://pubs.acs.org.

AUTHOR INFORMATION

Corresponding Author
rwm@email.unc.edu

Notes

The authors declare no competing financial interest.

ACKNOWLEDGMENTS

REFERENCES

(1) Chen, S.; Ingram, R. S.; Hostetler, M. J.; Pietron, J. J.; Murray, R. W.; Schaaff, T. G.; Khoury, J. T.; Alvarez, M. M.; Whetten, R. L. *Science* **1998**, *280*, 2098.

(2) Chen, S.; Murray, R. W.; Feldberg, S. W. *J. Phys. Chem. B* **1998**, *102*, 9898.

(3) Hicks, J. F.; Miles, D. T.; Murray, R. W. *J. Am. Chem. Soc.* **2002**, *124*, 13322.

(4) Murray, R. W. *Chem. Rev.* **2008**, *108*, 2688.

(5) Sardar, R.; Funston, A. M.; Mulvaney, P.; Murray, R. W. *Langmuir* **2009**, *25*, 13840.

(6) Kim, J. M.; Koo, C. M.; Kim, J. *Electroanalysis* **2011**, *23*, 2019.

(7) Ingram, R. S.; Hostetler, M. J.; Murray, R. W.; Schaaff, T. G.; Khoury, J. T.; Whetten, R. L.; Bigioni, T. P.; Guthrie, D. K.; First, P. N. *J. Am. Chem. Soc.* **1997**, *119*, 9279.

(8) Hostetler, M. J.; Templeton, A. C.; Murray, R. W. *Langmuir* **1999**, *15*, 3782.

(9) Templeton, A. C.; Hostetler, M. J.; Kraft, C. T.; Murray, R. W. *J. Am. Chem. Soc.* **1998**, *120*, 1906.

(10) Wolfe, R. L.; Balasubramanian, R.; Tracy, J. B.; Murray, R. W. *Langmuir* **2007**, *23*, 2247.

(11) Hostetler, M. J.; Green, S. J.; Stokes, J. J.; Murray, R. W. *J. Am. Chem. Soc.* **1996**, *118*, 4212.

(12) Cabo-Fernández, L.; Bradley, D. F.; Romani, S.; Higgins, S. J.; Schiffrin, D. J. *ChemPhysChem* **2012**, *13*, 2997.

(13) Chen, S. *Langmuir* **2001**, *17*, 6664.

(14) Stiles, R. L.; Balasubramanian, R.; Feldberg, S. W.; Murray, R. W. *J. Am. Chem. Soc.* **2008**, *130*, 1856.

(15) Sardar, R.; Beasley, C. A.; Murray, R. W. *Anal. Chem.* **2009**, *81*, 6960.

(16) Chow, K.-F.; Sardar, R.; Sassin, M. B.; Wallace, J. M.; Feldberg, S. W.; Rolison, D. R.; Long, J. W.; Murray, R. W. *J. Phys. Chem. C* **2012**, *116*, 9283.

(17) Mars, A.; Parolo, C.; Raouafi, N.; Boujlel, K.; Merkoci, A. *J. Mater. Chem. B* **2013**, *1*, 2951.

(18) Carducci, T. M.; Murray, R. W. *J. Am. Chem. Soc.* **2013**, *135*, 11351.

(19) Terrill, R. H.; Postlethwaite, T. A.; Chen, C.-h.; Poon, C.-D.; Terzis, A.; Chen, A.; Hutchison, J. E.; Clark, M. R.; Wignall, G. *J. Am. Chem. Soc.* **1995**, *117*, 12537.

(20) Wuelfing, W. P.; Green, S. J.; Pietron, J. J.; Cliffel, D. E.; Murray, R. W. *J. Am. Chem. Soc.* **2000**, *122*, 11465.

(21) McCreery, R. L. *Chem. Mater.* **2004**, *16*, 4477.

(22) Block, B. P.; Bartkiewicz, S. A.; Chrisp, J. D.; Gentile, P.; Morgan, L. O. *Inorg. Synth.* **1953**, *4*, 14.

(23) Glemser, O.; Sauer, H. In *Handbook of Preparative Inorganic Chemistry*, 2nd ed.; Brauer, G., Ed.; Academic Press: New York, 1963; Vol. 2, p 1057.

(24) Wolfe, R. L.; Murray, R. W. *Anal. Chem.* **2006**, *78*, 1167.

(25) Hostetler, M. J. *J. Am. Chem. Soc.* **1996**, *118*, 4212.

(26) Lee, D.; Donkers, R. L.; Wang, G.; Harper, A. S.; Murray, R. W. *J. Am. Chem. Soc.* **2004**, *126*, 6193.

(27) Bard, A. J.; Faulkner, L. R. *Electrochemical Methods: Fundamentals and Applications*, 2nd ed.; John Wiley & Sons: New York, 2001.

(28) Pietron, J. J.; Hicks, J. F.; Murray, R. W. *J. Am. Chem. Soc.* **1999**, *121*, 5565.

(29) Wuelfing, W. P.; Murray, R. W. *J. Phys. Chem. B* **2002**, *106*, 3139.

(30) Choi, J.-P.; Murray, R. W. *J. Am. Chem. Soc.* **2006**, *128*, 10496.

(31) Heaven, M. W.; Dass, A.; White, P. S.; Holt, K. M.; Murray, R. W. *J. Am. Chem. Soc.* **2008**, *130*, 3754.

(32) Hostetler, M. J.; Wingate, J. E.; Zhong, C.-J.; Harris, J. E.; Vachet, R. W.; Clark, M. R.; Londono, J. D.; Green, S. J.; Stokes, J. J.; Wignall, G. D.; Glish, G. L.; Porter, M. D.; Evans, N. D.; Murray, R. W. *Langmuir* **1998**, *14*, 17.

(33) Lopez-Acevedo, O.; Akola, J.; Whetten, R. L.; Grönbeck, H.; Häkkinen, H. *J. Phys. Chem. C* **2009**, *113*, 5035.

(34) Hicks, J. F.; Zamborini, F. P.; Osisek, A. J.; Murray, R. W. *J. Am. Chem. Soc.* **2001**, *123*, 7048.

(35) Snow, A. W.; Wohltjen, H. *Chem. Mater.* **1998**, *10*, 947.

(36) Guidez, E. B.; Aikens, C. M. *Phys. Chem. Chem. Phys.* **2012**, *14*, 4287.